

Focused bulk ultrasonic waves generated by ring-shaped laser illumination and application to flaw detection

Xiao Wang and Michael G. Littman

Department of Mechanical and Aerospace Engineering, Princeton University, Princeton, New Jersey 08544

John B. McManus

Aerodyne Research, Inc., Billerica, Massachusetts 01821-3976

Mohsen Tadi, Young Sik Kim,^{a)} Attila Askar,^{b)} and Herschel Rabitz

Department of Chemistry, Princeton University, Princeton, New Jersey 08544

(Received 15 December 1995; accepted for publication 25 June 1996)

Focused bulk ultrasonic waves have been generated in aluminum plates by surface irradiation with ring-shaped laser light. The waves are detected by a piezoelectric transducer. Compression and shear peak amplitudes drop quickly when the detector is moved away from the epicenter. This shows that strong focusing exists at the epicenter as the result of constructive interference of the waves generated by different parts of the ring. The focusing persists when the radius of the laser light is scanned over a large range, indicating that the elastic disturbance concentrates in depth along the ring's central axis. Numerical simulations are presented for comparison. The "pencil-like" acoustic wave structure is used to observe a sample plate with an artificial flaw. Strong new features including compress-shear mode conversion at the site of the flaw are observed. These features are used to locate the flaw within the sample. © 1996 American Institute of Physics. [S0021-8979(96)03319-1]

I. INTRODUCTION

Laser generation of acoustic waves offers significant advantages for studies of materials and structures [nondestructive evaluation (NDE)], especially since the waves can be produced in a noncontacting manner, with the point of generation easily moved across the surface of a test object. However, the technique of laser acoustic wave generation has the problem of producing relatively low acoustic amplitudes. The acoustic amplitude is limited because one usually wants to avoid melting or ablating the surface of the material under study. Much higher wave amplitudes can be reached under ablative conditions, with the sacrifice of surface material. The usual "photothermal" generation mechanism in testing applications is based on the rapid, but small, thermal expansion of a heated surface layer.^{1,2} Low intrinsic acoustic amplitudes increase the difficulty of detecting the generated or scattered waves. This is especially a problem for optical detection methods, such as interferometry, which have lower sensitivity than contacting piezoelectric transducers. Optical detection methods are preferable in many circumstances, due to their fully noncontacting nature.³

The difficulty of low acoustic amplitudes in laser acoustics can be relieved somewhat by taking advantage of constructive interference between waves generated by different parts of an acoustic source, giving locally higher amplitude. The acoustic source is then a pattern of laser illumination, designed in space and time. There have been numerous reports of designing laser patterns, either spatially or temporally for tailored acoustic generation.⁴⁻¹⁴ For example, Cielo

and co-workers⁴ used a ring-shaped irradiation pattern produced with an axicon and a pulsed laser to generate a convergent surface wave. They observed a factor of 20 signal level increase compared to surface waves generated by a line source, with equal surface heating. Others also have produced focused surface waves with pulsed illumination patterns.⁵⁻⁹ Beam steering can be accomplished with a set of precisely timed illumination points.¹⁰⁻¹⁴ For example, Noroy and co-workers¹⁰ generated steered acoustic waves by controlling the time delay among 16 individual YAG lasers, each focused into lines.

We have previously investigated the application of optimal control theory to the design of illumination patterns in laser acoustics.¹⁵⁻¹⁷ Optimal control theory (OCT) can be used to derive laser patterns that represent an optimized balance between driving the physical system to reach a specific goal and minimizing the costs of reaching the goal. We have investigated the design goal of pulsed acoustic focusing for maximizing the acoustic energy in a small subsurface volume at an instant in time, by means of a spatial-temporal pattern of forces on the surface of an isotropic elastic medium. The system costs were to minimize the total energy outside the focal volume, and to minimize the driving forces. The general result of such an optimization is a force pattern in the form of rings, which, in time, shrink or collapse toward the central axis. The collapsing rings' surface velocity varies, as determined by the propagation times of the generated waves to the subsurface focus.

Photothermal generation produces mainly shear waves, which (for pointlike sources) peak in amplitude at a fixed angle from the surface normal. This angle depends on the medium, and is just outside the critical angle, $\theta_c = \arcsin(v_s/v_c)$. For example, in aluminum, with $v_s = 0.304$ cm/ μ s and $v_c = 0.64$ cm/ μ s, the critical angle is

^{a)}Permanent address: Department of Applied Science, Hong-ik University, Mapoku, Seoul 121, Korea.

^{b)}Permanent address: College of Art and Sciences, Koc University, Bebek-Istanbul, Turkey.

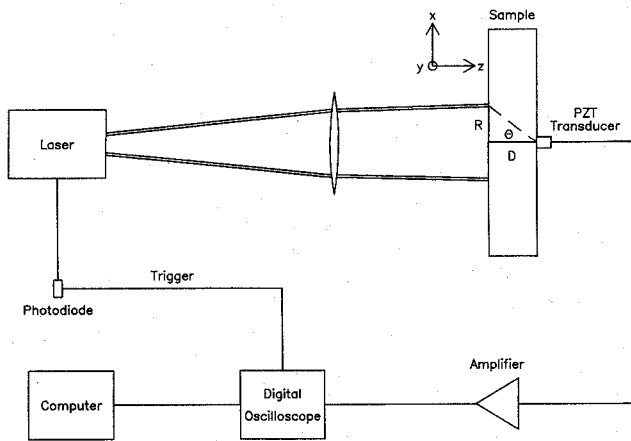


FIG. 1. Schematic diagram of the experimental setup and the ring geometry.

28.4°, and the shear waves peak at 30°.¹⁸ The characteristic angular pattern of photothermal waves implies that a substantial fraction of the energy delivered to the target is produced by rings with a narrow range of radius. This explains our earlier modeling prediction that a fixed ring does a reasonably good job of delivering acoustic energy to a subsurface volume.¹⁷ The nominal geometry under consideration is to set the ring radius so that the shear waves, at the angle of maximum amplitude (θ_{\max}), overlap on the ring axis. The angle of maximum shear amplitude implies an optimum ring radius for a specific focal depth

$$R_{\text{opt}} = (\text{focal depth}) \tan(\theta_{\max}),$$

or a maximum amplitude focal depth for a given radius (see Fig. 1).

There are two significant advantages to using ring-shaped laser illumination patterns in NDE applications. First, the acoustic waves come to a focus along the central axis of the ring, to give an increased amplitude at depth in the solid. Second, the ring form spreads the laser power across the surface, so that more total energy can be applied before the onset of melting or ablation, as compared to spot illumination.

In this article we report measurement of bulk ultrasonic waves generated in aluminum plates with irradiation of ring-shaped laser light. To our knowledge, experimental studies of the subsurface acoustic focusing properties of ring-shaped surface illumination have not been reported previously. We describe the experimental procedure and results in the following section. In Sec. III, we present numerical calculations as a comparison. Finally, in Sec. IV we discuss the results and their potential applications.

II. EXPERIMENT

We report here on experiments utilizing ring-shaped illumination for bulk acoustic wave generation. The experiments were based on an expectation of an acoustic focus on the axis of the ring, and with a maximum in depth near the depth of crossover of shear waves near the critical angle. The characteristics of the generated waves were measured with a contacting transducer on the back of a sample plate. Back-

surface measurements are a substitute for true internal measurements of the waves. However, additional phenomena are introduced in backsurface measurements, such as the sensitivity of the transducer only to the normal component of the displacement, and mode conversion of the waves upon reflection. Acoustic wave forms were recorded with the detector scanned across the back surface, and then as the ring radius was varied, with the detector on epicenter. Finally, in an additional study, the ring form was used to generate waves that were used to observe a flaw inside the sample.

Figure 1 is a schematic diagram of the experimental setup. We used a Q -switched $\text{Ti}:\text{Al}_2\text{O}_3$ laser operating at 800 nm, with 50 ns [full width at half-maximum (FWHM)] 80 kW pulses. The output of the laser was masked into a ring and projected upon the surface of the sample plate by a convex lens ($f.l. = 25$ cm). The ring radius was adjusted by changing the distance from the lens to the sample (z direction). The samples were aluminum plates, 100 mm square and various thicknesses, with machine-finished (bare) surfaces. The elastic waves generated by the absorption of the laser pulse propagated through the plate and were detected by a 3-mm-diam PZT transducer (Panametrics V-129) on the back surface. The transducer sensitivity peaks at 9.8 MHz, with 6 dB bandwidth of 10 MHz. It was mounted on a two-dimensional translation stage, and could be scanned in both x and y directions. The transducer was spring loaded softly against the surface. A silicone coupling oil was used.

The sample plate was mounted on a translation stage and could be independently scanned in the x direction. The laser output energy was kept constant at about 4 mJ/pulse, with intensity at the sample of $\approx 3 \times 10^6$ W/cm². In the reported cases below, measurements were made ten times at each designated location. Each of the ten measurements involved the movement of the transducer away from the designated location and back again in order to minimize the variation of detection coupling efficiency. Typically runs consisted of 120 laser shots for each of the ten individual measurements. Neither ablation nor surface damage was observed. Ultrasonic wave forms detected by the transducer were amplified (HP 462A) and recorded by a digital oscilloscope (LeCroy 9410), which also averages the signal.

In the first experiment, we probed the transverse structure of the generated waves, while operating near the ring angle that corresponded to the expected maximum acoustic amplitude. In this case, the sample thickness was 12.7 mm and the mean radius (approximately R_{opt}) of the laser ring was 8.0 mm, corresponding to a ring angle of 32°. The ring thickness was approximately 0.5 mm, which is comparable to the compression wave wavelength at 10 MHz in aluminum. Data were also collected for ring radii greater and less than R_{opt} , at 10 and 5 mm. For a set ring radius, the transducer was scanned across the back surface (in the x direction) to measure the normal surface displacement induced by the elastic waves.

Examples of recorded wave forms from the first experiment are shown in Fig. 2. In Fig. 2(a), with the transducer at the epicenter relative to the ring, a sharp rise at 2.4 μs represents the arrival of the compressional waves, followed by a peak with larger amplitude at 4.9 μs that represents the shear

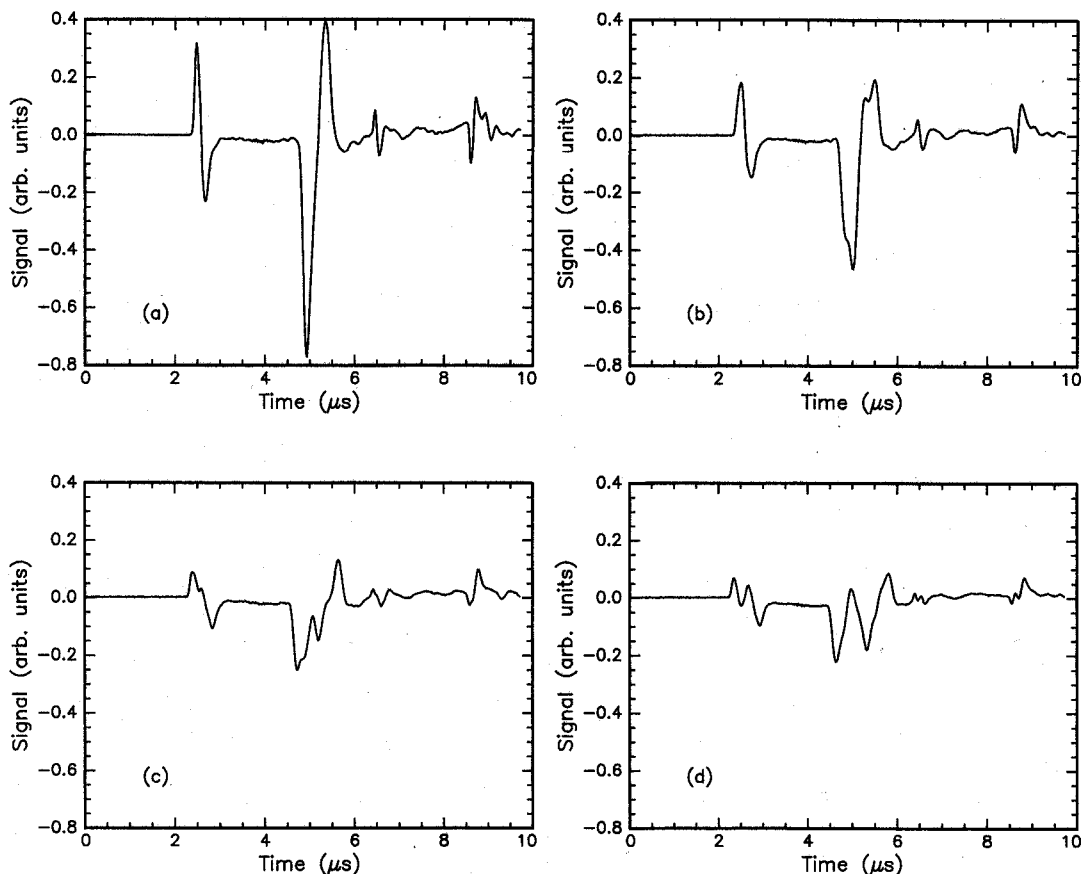


FIG. 2. Recorded rear surface wave forms for a 12.7 mm plate illuminated by an 8-mm-radius ring (R_{opt}). The transducer location is: (a) the epicenter; (b) 1 mm; (c) 2 mm; and (d) 3 mm from epicenter.

wave arrival. Two more features follow at 6.4 and 8.6 μ s, which are due to reflections between the back and front surfaces of the sample. In Figs. 2(b) and 2(c), as the transducer is moved to off center locations, the signal amplitude drops rapidly, since waves created by different portions of the ring no longer reinforced by arriving at the detector at the same time. Finally, in Fig. 2(d), where the transducer is 3 mm off the epicenter, the sharp shear and compression peaks each splits into two separated peaks whose amplitudes are only 25% of that of the original peaks.

Figure 3 plots the shear wave amplitude as a function of distance from the epicenter for three different ring radii. The shear wave amplitude here is obtained in the same manner as in Ref. 3. The amplitude is the magnitude of the downward step in signal at the onset of the shear wave arrival at the transducer. For measurement positions off the epicenter, for which there is a range of shear wave arrival times, we plot the shear amplitude over an appropriate time window. Sharp focusing at the epicenter is evident in all cases. The radius for the falloff of the amplitude by a factor of 1/2 is approximately 1.5 mm. This measured focal radius is comparable to the size of the transducer, so the actual focal radius is somewhat less than 1.5 mm. We expect the focal radius to be comparable to the ring thickness.

In the next experiment, we varied the ring radius while the transducer was in a fixed position on the epicenter of the ring. This was intended to probe the characteristics of the

focus in depth. Since we cannot directly probe the interior, we rescaled the geometry by changing the relative dimensions of the ring and sample thickness. In this case, the sample was a 19-mm-thick aluminum plate.

Figure 4 shows (a) the resulting shear and (b) compressional wave amplitudes at the epicenter as a function of ring

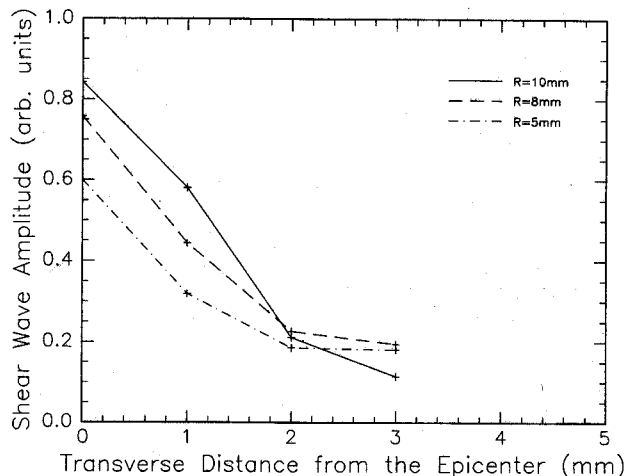


FIG. 3. Shear wave amplitude at different detector locations and for three different ring radii. Plate thickness: 12.7 mm.

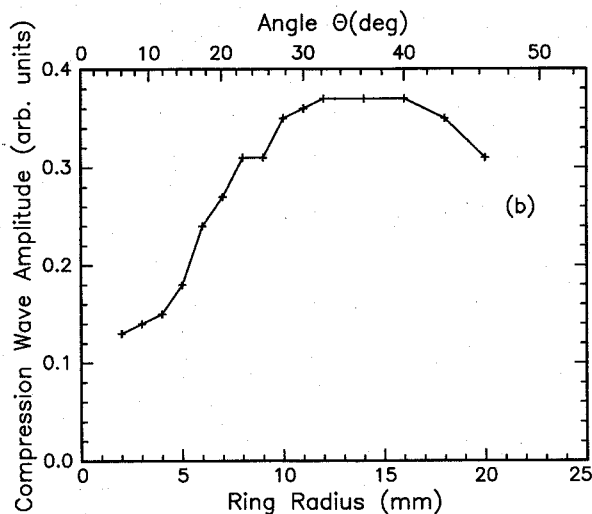
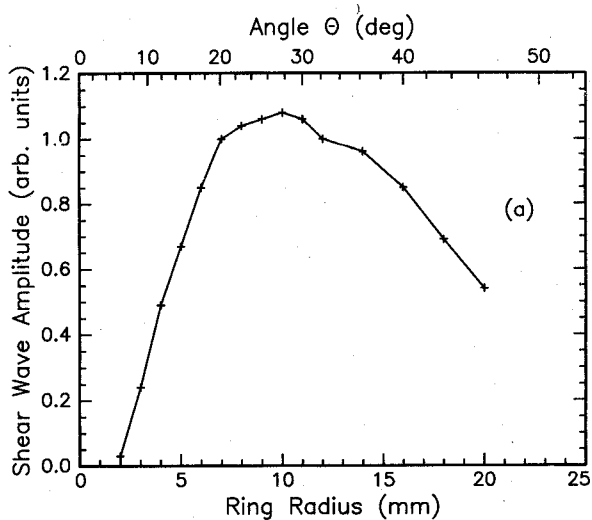


FIG. 4. Back surface shear and compression wave amplitude as a function of ring radius, for a 19-mm-thick plate. (a) Measured shear wave amplitude as a function of ring radius. (b) Similar plot for compression wave amplitude.

radius. At small ring radius the illumination pattern is similar to a spot, and the shear wave amplitude approaches zero, consistent with other reports.¹⁸ As the ring radius increases, the shear wave amplitude also increases, and reaches the maximum at ring radius of 10 mm, corresponding to a ring angle of 28° [see Fig. 5(a)]. This is close to the expected¹⁸ shear θ_{\max} of 30° for a thermoelastic point source in aluminum. The observed shear wave amplitude remains high for a large range of angles, unlike that generated by a point source. This is due to convergence of waves on the central axis. The shear amplitude falls off sharply for ring radius less than 4 mm, which would correspond to a focal depth of 7.6 mm for the shear waves at θ_{opt} . Thus, the sharp focus persists for 2.5 times the depth as would be expected from the simple picture of overlap of the peak amplitude shear waves. The picture that this suggests is a “pencil-like” focus, with the elastic waves staying highly focused along the epicenter for almost the entire depth of the plate. Our observation that the compressional component is less focused than the shear

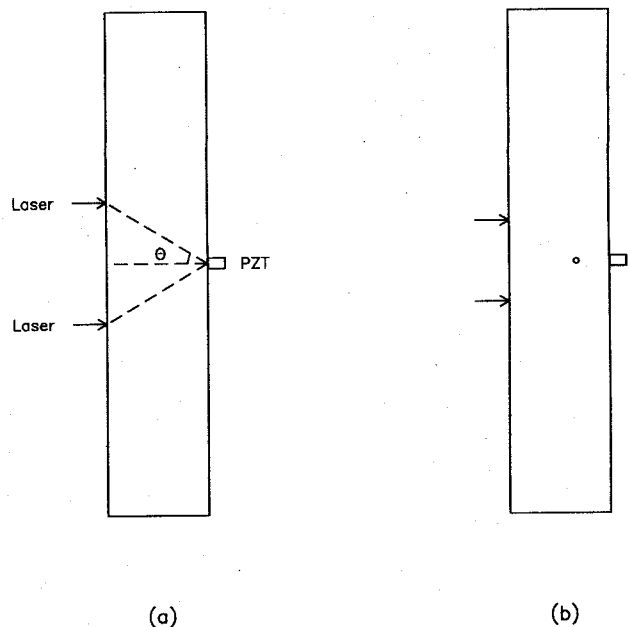


FIG. 5. (a) Cross section of the sample, and (b) sample with an artificial defect hole.

component is consistent with known compressional/shear directivity patterns such as those noted in Ref. 3.

As a final experiment to demonstrate the focal characteristics of acoustic waves generated by a ring, we compared the results of wave generation by a spot, with the same fluence and the same offset angle as was used at the optimum ring radius. We compared the signal from a small section of a ring to that from a full ring, with diameter 10 mm and width 0.5 mm, on a 19-mm-thick plate. The signal scaled linearly with the linear length of the ring used. Thus, for a ring radius of 10 mm and thickness of 0.5 mm, the signal for the full ring is more than 100 times greater than for a spot with diameter equal to the ring thickness.

The acoustic waves generated by ring-shaped photothermal excitation may be applied to the detection of internal defects. The sharp lateral focus of the internal waves, which persists for some depth, suggests that one can use this setup to detect internal defects with good spatial resolution. The large shear wave amplitude produced by this method also suggests that defect detection can be carried out by shear to compression mode conversion.

We created an artificial subsurface defect in the plate by drilling a 2.3-mm-diam hole from the side wall, along the y direction, and examined it with ring-shaped source. The flaw was centered 13.2 mm from the front surface of the 19-mm-thick plate [see Fig. 5(b)]. The ring radius was 7.7 mm, which corresponded to a nominal focal depth of 13 mm. We scanned the flaw location through the ring axis, by moving the plate in the x direction while both the ring and the transducer were kept stationary.

Figure 6 shows the recorded wave forms for different defect locations. Compression–compression and shear–shear scattering by the defect are present, as indicated by the distortion of the compression arrival peak at 3.3 μs and shear arrival peak at 6.5 μs . These features are too close to the

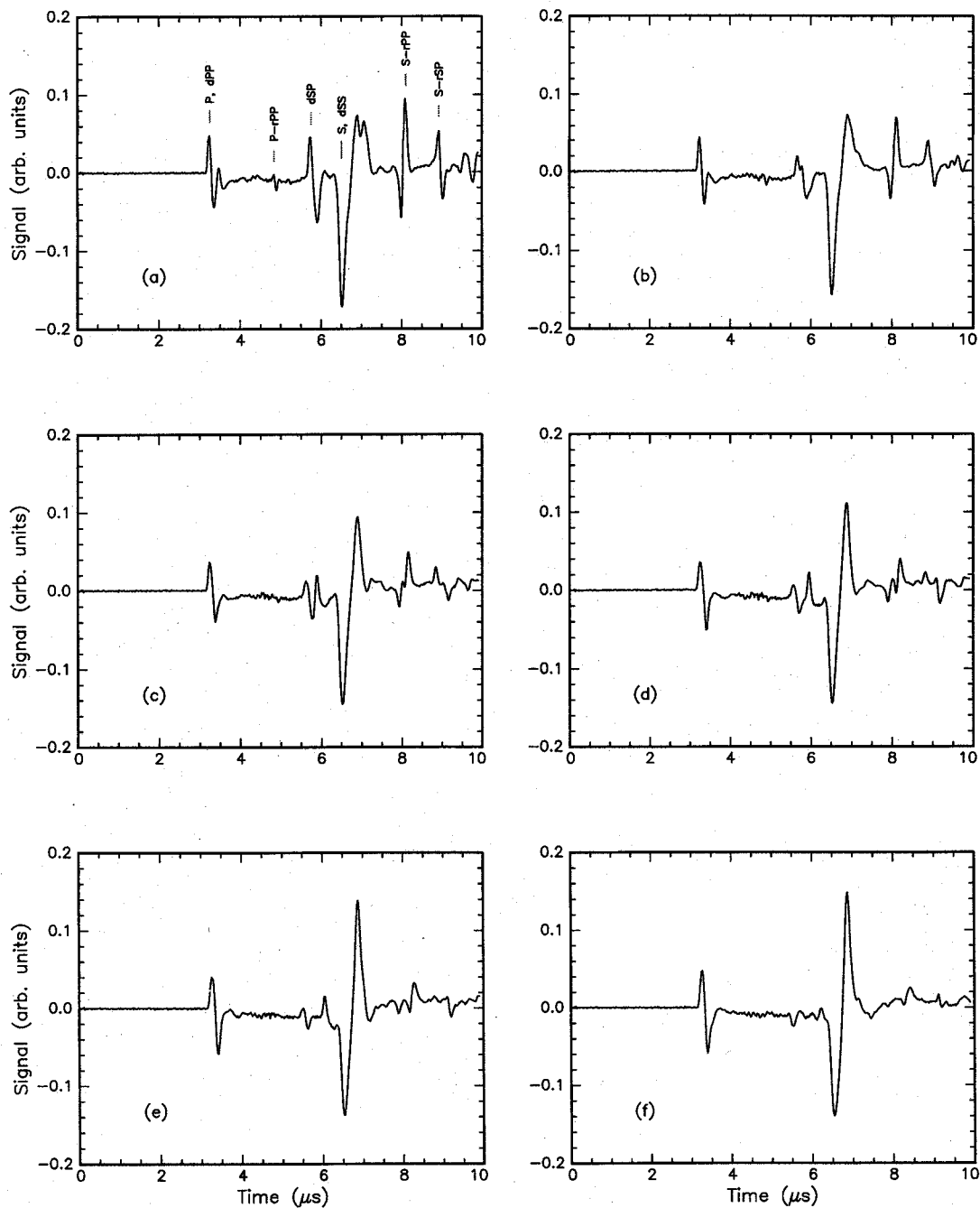


FIG. 6. Recorded wave forms for different defect locations: (a) center; (b) 0.5 mm off center; (c) 1 mm off center; (d) 1.5 mm off center; (e) 2 mm off center; and (f) 3 mm off center.

existing peaks to be used to identify the defect location.

Four more pronounced new features due to the presence of the defect appear in Fig. 6(a). The first feature occurring at $4.8 \mu\text{s}$ is the arrival of the compression wave reflected first by the back surface and then by the defect. This feature is labeled as P-rPP, following the notation of Scruby *et al.*^{3,19} [see Fig. 6(a)]. The second feature occurring at $5.7 \mu\text{s}$, labeled dSP, is due to shear to compression mode conversion at the defect, with the scattered compressional wave reaching the transducer before the direct shear waves arrive. The third feature at $8.1 \mu\text{s}$, labeled as S-rPP, is caused by shear waves converted into compression waves at the back surface and then reflected by the defect. The last feature at $8.9 \mu\text{s}$, la-

beled as S-rSP, is the shear-shear reflection at the back surface of the plate, which then scatters off the defect as a compression wave.

The location of the defect can be calculated by measuring the timing of the above mentioned new wave-form features in Fig. 6(a), and using the known speeds of shear and compression waves in aluminum. The flaw distance from front surface determined from the four new features are: 14.1, 12.6, 14.2, and 14.0 mm. Notice that the second-listed depth is smaller than the other three, because the first-, third-, and fourth-listed depths all derive from the back surface of the defect, which is at 14.4 mm from the front surface of the plate. The average, 13.7 mm, is very close to the actual 13.2

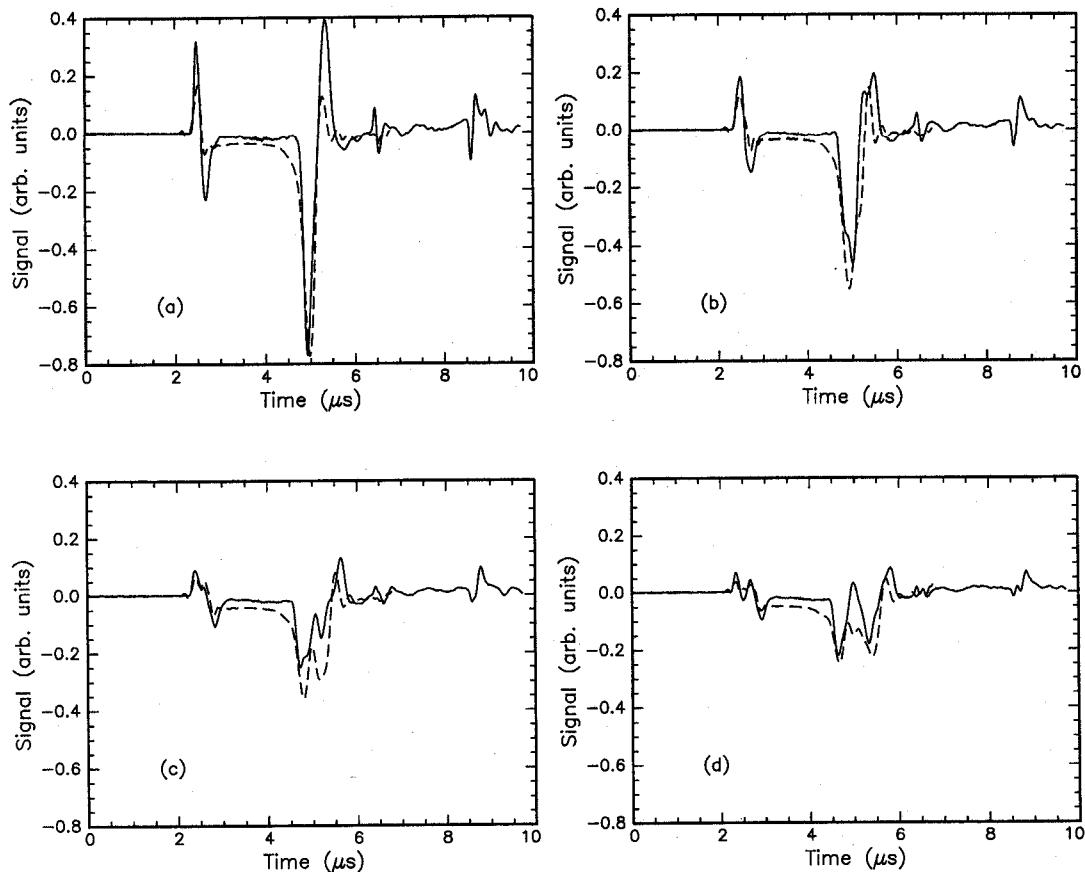


FIG. 7. Experimental and modeled rear surface displacement wave forms for transducer at (a) the epicenter; (b) 1 mm, (c) 2 mm, and (d) 3 mm from the epicenter.

mm, with the error within the radius of the hole. Figures 6(b)–6(f) show that the amplitudes of the new peaks due to the defect decrease rapidly when the defect is moved away from the central axis, as expected from the tight focusing along the axis.

The combination of a tight focus along the central axis plus time of flight analysis of the mode-converted scattered waves is suitable for mapping out defect locations or contours. Defect detection by mode conversion was reported by Scruby and co-workers, with a thermoelastic point-like source, and both the source and the receiver on the same side of the sample plate.¹⁹ The maximum defect signal was with the source offset from the defect, due to the angular distribution of generated waves. Complicated data processing was necessary due to the geometry. In the present case, because of the intrinsic symmetry of the arrangement, locating a defect can be easier. The axis of the ring provides the highest amplitude for defect scattering, and the detected wave form is most symmetrical when the defect is on the axis.

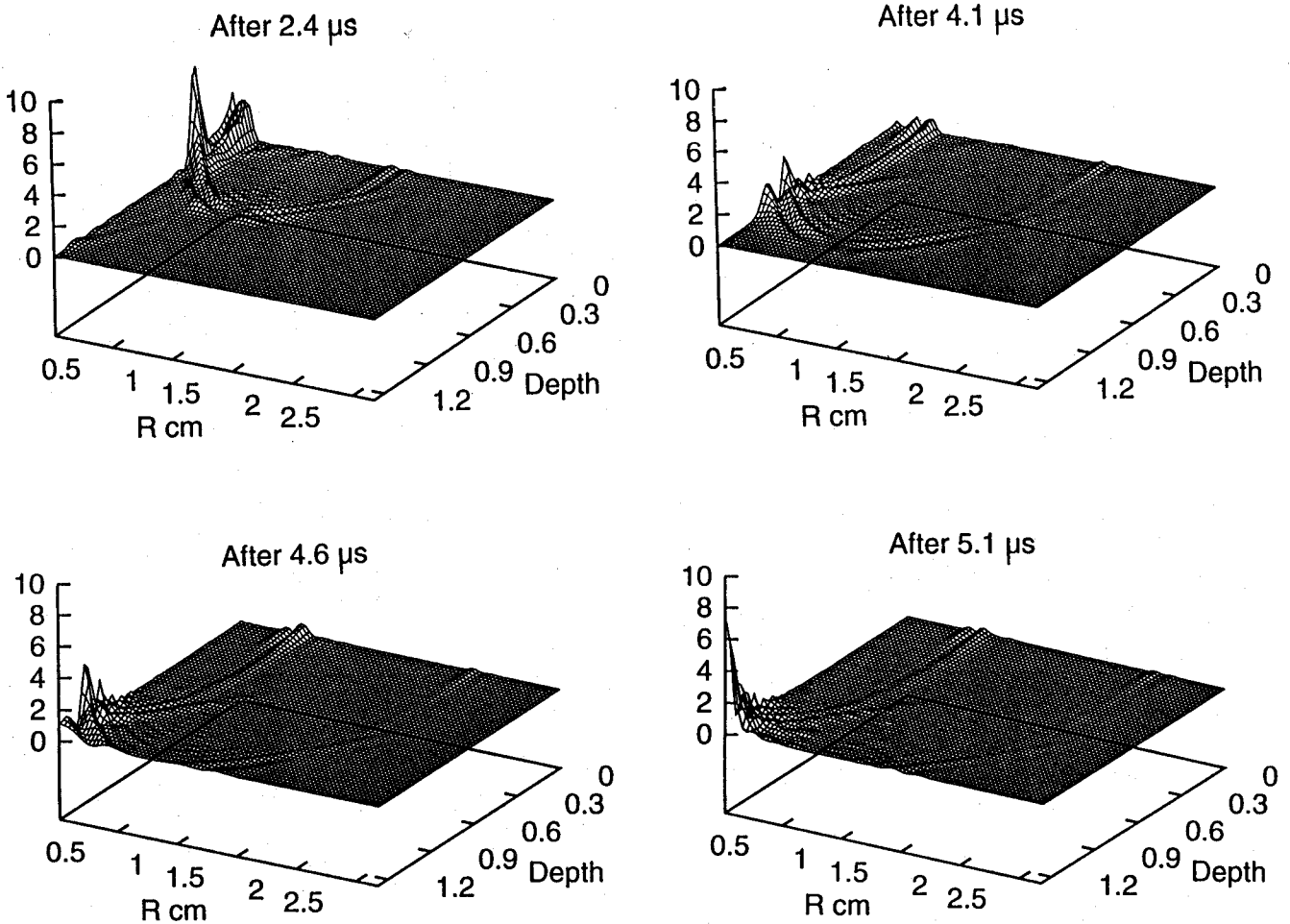
III. COMPARISON WITH THEORY

Optimal control theory applied to photothermal wave generation has been used to demonstrate that a fixed ring works reasonably well at delivering acoustic energy to a sub-surface volume.¹⁷ The OCT modeling was done with a Green's-function description of the semi-infinite solid, and did not have wave reflection features due to the infinite ex-

tent of the geometry. Therefore, we have examined this nearly optimal solution as a fixed ring at an optimal angle with a numerical model of wave propagation through the solid. This gives a complete picture of the wave structure and energy density throughout the volume and at the back surface. The time history of the normal displacement at the back surface is computed and compared to experiments.

In this section we describe a model elastic solid whose surface is irradiated by a ring-shaped incident laser beam. The applied heat generates thermal stresses in the solid adjacent to the surface. These stresses in turn generate compression and shear waves that propagate into the solid much faster than the heat diffusion process. Moreover, the time duration of laser pulse is much smaller than the time required for the heat to significantly diffuse into the solid. Therefore, the solid can be divided into two regions. In the top region thermal effects are present, and the material is assumed to be thermoelastic. In the bottom region thermal effects are ignored and the material is assumed to be purely elastic. At the boundary between the two regions the displacement and its first derivative are required to be continuous. The equations of motion for the top region are given by

$$\rho c_v \frac{\partial T}{\partial t} - K \frac{\partial^2 T}{\partial x_i \partial x_i} = h(t, x_1, x_2) \delta(x - x_3), \quad (1)$$



Energy Density Contours in $10^{-3} \times \frac{\text{J}}{\text{cm}^3}$

FIG. 8. Snapshots of computed elastic energy density in the sample at (a) 2.4 μs , (b) 4.1 μs , (c) 4.6 μs , and (d) 5.1 μs after the elastic wave is launched.

$$\mu \frac{\partial^2 u_i}{\partial x_j \partial x_j} + (\lambda + \mu) \frac{\partial^2 u_j}{\partial x_j \partial x_i} - \alpha(3\lambda + 2\mu) \frac{\partial T}{\partial x_i} = \rho \ddot{u}_i, \quad (2)$$

where $T(t, x_i)$ is the temperature, $u_i(t, x_i)$ the displacements, λ, μ are Lamé's constants, K the thermal conductivity, ρ the mass density, c_v the specific heat, and α the thermal expansion coefficient. The incident laser is modelled as a surface heat source $h(t, x_1, x_2)$. Given $h(t, x_1, x_2)$, the temperature field can be obtained independently using the heat conduction equation. The thermal expansion is then generated by the imposed temperature field through the second equation. The conversion of elastic energy to thermal energy is ignored and the temperature rise is considered to be due to the incident laser only. For the lower region, the thermal field in Eq. (2) is ignored due to the much slower propagation of thermal diffusion compared with elastic waves. Thus, we have

$$\mu \frac{\partial^2 u_i}{\partial x_j \partial x_j} + (\lambda + \mu) \frac{\partial^2 u_j}{\partial x_j \partial x_i} = \rho \ddot{u}_i. \quad (3)$$

The computations are done using the code DYNFLOW.²⁰ The calculations are based on the physical properties of an

aluminum alloy: $\rho = 2.77 \text{ g/cm}^3$; $\lambda = 0.546 \times 10^{12} \text{ g/cm s}^2$; $\mu = 0.257 \times 10^{12} \text{ g/cm s}^2$; $K = 2.37 \text{ J/cm}$; $c_v = 1 \text{ J/g}$, and $\alpha = 24 \times 10^{-6} \text{ C}^{-1}$. Details of the theoretical formulation, the numerical procedure, and other case studies will be presented elsewhere.²⁰ In the application of DYNFLOW modeling, the spatial mesh was rather coarse, due to limitations of computer memory. This resulted in residual numerical oscillations in the computed wave forms, of as much as 20% of the peak displacements.

Figure 7 shows calculated rear surface normal displacement wave forms for four different locations of the detector, moving to the side of epicenter. These results are for a 12.7-mm-thick plate and a fixed ring radius of 8 mm, corresponding to the first experiment. Comparing the experimental wave forms in Fig. 2 to those in Fig. 7, in all cases the calculation correctly predicts the location and the polarity of the measured wave-form peaks. Also, the amplitudes of shear and compression wave transients agree reasonably well. Thus, the modeling supports the observed transverse focusing at the rear surface.

Figure 8 presents "snapshots" of computed elastic energy density in the sample at several different times after the elastic waves are launched. This corresponds to a 12.7-mm-thick plate and a ring radius of 7.3 mm, with the ring angle 29.9° . It can be seen that the energy concentrates around the epicentral axis, after the shear waves begin to overlap. The intense energy peak is also well defined in z direction, in each time epoch shown. When the pulse reaches the back surface, the waves reflect and the energy peak breaks up. The model predicts that the epicenter shear peak amplitude has a broad maximum at a ring angle of 35° ; however, the experimental maximum shear ring angle is somewhat smaller, at 29° . This difference may be associated with spatial averaging nature of the detector.

IV. CONCLUSIONS

We have experimentally demonstrated strong lateral focusing of elastic waves at the epicenter with waves generated by a ring-shaped light source. This is supported by the results of numerical simulation. Both the experiment and the numerical simulation results show that the elastic waves are narrowly confined near the epicentral axis. Thus, effective focusing in depth of the elastic waves can be achieved with this simple configuration. Furthermore, the waves are not narrowly focused at a single depth, which can facilitate the process of locating defects at unknown depths. Strong converging waves may be useful for detection of oriented flat cracks and flaws.

The waves might be further confined along the epicentral axis by adding more control to the ring load, namely, sweeping the radius of the ring with a speed that matches the elastic wave speed in the sample, so that constructive interference occurs only at a target location that is well defined in all three dimensions.^{15,16} The use of OCT provides a means to design the optimal loads for this purpose. We are currently working on an electro-optical sweeping device that may be used for this purpose.

ACKNOWLEDGMENTS

The authors would like to thank J. H. Prevost for permission of using his DYNFLOW code, and for many useful discussions. This work was supported by the U.S. Department of Energy under Contract No. DE-FG02-93ER12129.

- ¹C. B. Scruby, R. J. Dewhurst, D. A. Hutchins, and S. B. Palmer, *J. Appl. Phys.* **51**, 6210 (1980).
- ²D. A. Hutchins, *Can. J. Phys.* **64**, 1247 (1986).
- ³C. B. Scruby and L. E. Drain, *Laser Ultrasonics Techniques and Applications* (Adam Hilger, New York, 1990).
- ⁴P. Cielo, F. Nadeau, and M. Lamontagne, *Ultrasonics*, **55** (1985).
- ⁵C. K. Jen, P. Cielo, J. Bussiere, F. Nadeau, and G. W. Farnwell, *Appl. Phys. Lett.* **46**, 241 (1985).
- ⁶R. J. von Gutfield, D. R. Vigliotti, C. S. II, and W. R. Scott, *Appl. Phys. Lett.* **42**, 1018 (1983).
- ⁷R. D. Costley and Y. H. Bethelot, in *Review of Progress in Nondestructive Evaluation*, edited by D. O. Thompson and D. E. Chimenti (Plenum, New York, 1993), p. 579.
- ⁸H. Nakano and S. Nagai, *Ultrasonics* **29**, 230 (1991).
- ⁹R. C. Addison, L. J. Graham, R. S. Linebarger, and B. R. Tittman, in *IEEE Ultrasonics Symposium, 1987*, p. 1109.
- ¹⁰M. H. Noroy, D. Royer, and M. Fink, *Appl. Phys. Lett.* **63**, 3276 (1993).
- ¹¹M. H. Noroy, D. Royer, and M. Fink, *J. Acoust. Soc. Am.* **94**, 1934 (1993).
- ¹²J. W. Wagner, A. D. McKie, J. B. Spicer, and J. B. Deaton, *J. Nondestruct. Eval.* **9**, 263 (1990).
- ¹³A. J. A. Bruinsma and J. A. Vogel, *Appl. Opt.* **27**, 4690 (1988).
- ¹⁴K. Yamanaka, Y. Nagata, and T. Koda, *Appl. Phys. Lett.* **58**, 1591 (1991).
- ¹⁵Y. S. Kim, H. Rabitz, A. Askar, and J. B. McManus, *Phys. Rev. B* **44**, 4892 (1986).
- ¹⁶Y. S. Kim, H. Rabitz, M. Tadi, A. Askar, and J. B. McManus, *Int. J. Eng. Sci.* **33**, 907 (1995).
- ¹⁷Y. S. Kim, M. Tadi, H. Rabitz, A. Askar, and J. B. McManus, *Phys. Rev. B* **50**, 15 774 (1994).
- ¹⁸D. A. Hutchins, R. J. Dewhurst, and S. B. Palmer, *J. Acoust. Soc. Am.* **70**, 1362 (1981).
- ¹⁹C. B. Scruby, K. R. Jones, and L. Antoniazzi, *J. Nondestruct. Eval.* **5**, 145 (1987).
- ²⁰M. Tadi, A. Askar, and H. Rabitz (unpublished).